RSC Advances

ROYAL SOCIETY OF CHEMISTRY

www.rsc.org/advances

Journal Name

ARTICLE

Electrochemical deposition of Fe_2O_3 in the presence of organic additives: A route to enhanced photoactivity

Received 00th January 20xx,
Accepted 00th January 20xx

DOI: 10.1039/x0xx00000x

www.rsc.org/

Dereje H. Taffa,[a]* Ines Hamm,[b] Christian Dunkel[a], Ilya Sinev[b], Detlef Bahnemann,[c,d] Michael Wark[a]*

Abstract : The photoelectrochemical activity of hematite films prepared by electrochemical deposition (ED) in the presence of organic additives is discussed. The studies focus on the role of small organic additive molecules in tuning the morphology of the films and their influence on the photoelectrochemical oxidation of water. The organic additives, namely, coumarin 343 (C343), γ-glucuronic acid (GA) and sodium dodecyl sulfonate (Sds), possess functional moieties to interact with iron ions in the ED bath electrostatically or through metal-ligand complexation reaction. XPS measurements proof the incorporation of the organic additives, and oxidation states of Fe^{+3} ruling out the presence of mixed valences in the film. SEM and XRD measurements present morphological and structural evidence, respectively. The photoelectrochemical study shows organically modified hematite films exhibit enhanced photoactivity; the photocurrent density at 1.4V vs. RHE on GA-modified electrode is up to 5-6 times higher than on the unmodified electrode. Electrochemical impedance results reveal the role of the organic additives in reducing the charge transfer resistance from the hematite surface to the solution. In addition, a simple Ti post treatment greatly enhances the photoactivity of all electrodes under investigation.

Introduction

Solar energy is realized as one of the most promising renewable energy source which can potentially meet the increasing need of energy globally. [1] Since the seminal work of Fujishima and Honda the direct splitting of water using a photoelectrochemical cells (PEC) is an elegant way of storing energy in chemical bonds which is available on demand. [2-4] The solar irradiated semiconductor surface is the crucial part of the PEC device under stringent requirements. These criteria include chemical stability (in alkaline electrolytes), significant visible light harnessing ability, suitable band edge alignment to perform the water oxidation or reduction reactions, low production cost and good catalytic activity. [5] Among the promising candidates hematite (α-Fe_2O_3) fulfils most of the decisive factors and received considerable research interest. [6-10] With a band gap of 2.0-2.2 eV hematite is able to absorb a significant part of the solar spectrum (~40%), it is quite stable under illumination in aqueous solution and the valence holes are energetic enough to drive the water oxidation reaction. [11] However, the performance of hematite photoanodes is considerably low in contrast to the theoretical predictions. [8,12] Factors limiting the efficiency include short hole diffusion length, long light absorption cross section, and mismatch of the conduction band edge for the water reduction. [13-14]These shortcomings are addressed by nanostructuring to improve light absorption and charge collection [15-19] and doping [20-21] to enhance charge carrier density. Additionally, oxygen evolution catalysts [22-23] and passivation layers [24-25] are employed to decrease the overpotential of the multistep $4e^-$ oxygen evolution reaction which is inherently sluggish on hematite photoelectrodes.

Hematite photoanodes can be prepared following several strategies such as sol-gel [26], spray pyrolysis [27-28] chemical vapour deposition (CVD) [15,29] sputtering [19], atomic layer deposition (ALD) [30-31] and electrodeposition (ED) [32-34]. ED presents numerous attractive features over the other techniques such as the use of non-toxic iron precursors, simple instrumentation, high flexibility in terms of composition and experimental parameters, and easy scale up for fabrication of large area electrodes. Both cathodic and anodic ED routes for the preparation of α-Fe_2O_3 are reported. [35-36] The co-deposition of dopants such as Mo, Cr, Zr and Ni using the same α-Fe_2O_3 ED bath has been demonstrated by several research groups. [37-39] Inverse opal α-Fe_2O_3 photoanodes prepared via ED show outstanding performance. [40]

[a] Institute of Chemistry, Technical Chemistry, Carl von Ossietzky University Oldenburg Carl-von-Ossietzky-Str. 9-11, 26129 Oldenburg, Germany, E-mail: dereje.hailu.taffa@uni-oldenburg.de, Michael.wark@uni-oldenburg.de
[b] Faculty of Chemistry and Biochemistry, Laboratory of Industrial Chemistry, Ruhr-University Bochum, Universitaetsstr. 150, 44801 Bochum, Germany
[c] Institute of Technical Chemistry, Leibniz Universitaet Hannover, Callinstr 3, 30167, Hannover, Germany
[d] Laboratory for Nanocomposite Materials, Department of Photonics, Faculty of Physics, Saint-Petersburg State University, Ulianovskaia Str.3, Peterhof, Saint-Petersburg 198504, Russia.
Electronic Supplementary Information (ESI) available: SEM images, UV-Vis spectra, I-V curves, XPS and EDX data. See DOI: 10.1039/x0xx00000x

In this study we present anodic ED of hematite thin films in the presence of small organic molecules (capping or complexing agents) (Scheme 1). Previously we demonstrated the use of different dye and surfactant molecules in the ED of ZnO films to tune the porosity, surface area and morphology of the resulting films. [41-42] However, to the best of our knowledge such synthesis route and effect on the photoactivity of hematite photoanode was not reported. The molecules used in this study possess functional moieties, i.e. carboxylic acid groups, to interact with iron ions in the ED bath electrostatically or via metal-ligand complexation reaction. As deposited films are amorphous and can be converted to transparent crystalline α-Fe_2O_3 by annealing. The organic molecules influence the size and shape of the crystallites thereby affecting the photoelectrochemical performance. Structural and morphological evidence is presented from XRD and SEM measurements.

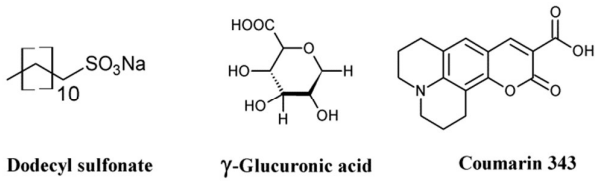

Dodecyl sulfonate γ-Glucuronic acid Coumarin 343

Scheme 1. Structure of organic additives used for ED of hematite films.

Experimental

Materials and Reagents

Ammonium iron (II) sulfate hexahydrate, sodium acetate, cobalt (II) nitrate tetrahydrate, coumarin 343 (C343), γ-glucuronic acid (GA) were analytical grade and purchased from Sigma-Aldrich and used as received. Sodium dodecyl sulfonate (Sds), potassium hydrogen phosphate, and potassium di-hydrogen phosphate were purchased from Roth, and titanium (IV) butoxide ($Ti(OBu)_4$) from Fluka. Conductive fluorine doped tin oxide (FTO) coated glass (15 Ω/sq) was purchased from Pilkington Germany.

Preparation of hematite photoelectrodes

FTO substrates were cleaned by sequential sonication in 0.1M NaOH, 0.1 M HCl, ethanol, and acetone, each for 10 min in an ultrasonic bath. Prior to each sonication step the FTO substrates were rinsed with distilled water and finally dried by N_2 blowing. ED of hematite thin films was carried out with an AMEL Potentiostat/Galvanostat 7050 interfaced with a computer running under Junior Assist software for Windows, version V3 (AMEL, Italy). For the ED experiments a conventional three electrode electrochemical cell with FTO glass as a working electrode, coiled Pt wire as counter electrode and an Ag/AgCl (XR300 Radiometer Analytical, sat. KCl) electrode separated by a salt bridge as a reference electrode was used. The deposition bath consist of 0.1 M CH_3COONa, 1mM of the organic additives and 0.02 M $(NH_4)Fe(SO_4)_2 \cdot 6H_2O$. and was bubbled with N_2 for 10-15 min. ED was performed potentiostatically at 0.4 V and the bath temperature was kept at 45 ^oC. The amount of charge was fixed to 0.3 C to obtain the same amount of photoactive material. Then the films were rinsed with distilled water and N_2 dried. The as prepared films were annealed at 600 ^oC for 1hour with temperature ramp of 2 ^oC/min.

Ti doping is performed by drop casting a solution of 25 µL $Ti(OBu)_4$ in absolute ethanol on to ED iron oxide films prior to thermal treatment. The cobalt phosphate (Co-Pi) was deposited potentiostatically at 0.9 V vs. Ag/AgCl from a solution of 0.5 mM $Co(NO_3)_2.6H_2O$ in 0.1 M phosphate buffer.

Structural characterization

UV-Vis Measurements: Diffuse reflectance spectra were recorded using a Cary 4000 spectrophotometer (Varian) equipped with an integrating sphere.

X-ray diffraction: Grazing incidence X-ray diffraction (GI-XRD) measurements were performed on a PANalytical X-ray diffractometer X'Pert PRO using Cu-Kα (1.54^{o}A) X-ray radiation. X-ray diffractograms were recorded over a range of 15-70 in 2θ.

Raman Measurements: Micro Raman measurements were carried out using SENTERRA Raman microscope (Bruker) equipped with 633 nm laser source.

Scanning Electron Microscopy: Scanning electron microscopy (SEM) measurements were performed on a Helios NanoLab 600i (FEI, Eindhoven, The Netherlands). Hematite films were cut and affixed with carbon conductive tape on aluminium sample holders. SEM images were recorded using a secondary electron detector at an acceleration voltage of 15.0 kV and a working distance of about 4 mm.

X-ray photoelectron spectroscopy: X-ray photoelectron spectroscopy (XPS) measurements were carried out in an ultra-high vacuum (UHV) set-up equipped with a monochromatic Al Kα X-ray source (hv = 1486.6 eV), operated at 14.5 kV and 35 mA, and a high resolution Gammadata-Scienta SES 2002 analyzer. The base pressure in the measurement chamber was maintained at about 7 × 10−10 bar. The measurements were carried out in the fixed transmission mode with pass energy of 200 eV resulting in an overall energy resolution of 0.25 eV. The high resolution spectra for the C 1s, O 1s and Fe 2p photoelectron lines were recorded. The binding energy scales were corrected to the charge shift by referring the most intensive sp2 hybridized C 1s contribution to 284.5 eV.

Photoelectrochemical measurements

All photoelectrochemical measurements were performed with a Zahner Zennium potentiostat using Thales software. The electrolyte was either 1 M NaOH (pH=13.6) or 0.1 M NaOH containing 0.5 M H_2O_2 (pH=12.5). Platinum wire and Ag/AgCl (sat. KCl) used as counter electrode and reference electrode, respectively. Hematite coated FTO served as working electrode; electrical contact was made using the bare FTO surface through a copper tape and the illumination area (2.54 cm^2) was defined with an O-ring. Light enters the cell from the electrolyte side through a quartz window (front side illumination). The light source is equipped with a calibrated white LED controlled by a second power potentiostat (Zahner

PP211). The output power can be varied between 10-100 mW cm^{-2}. Current-voltage (I-V) curves were recorded at a rate of 10 mV/s from -0.4V to +1.0V vs. Ag/AgCl (sat. KCl) in the dark and under illumination. Potential values were converted to the reference reversible hydrogen electrode (RHE) using the relationship (eq 1)

$$E_{RHE} = E_{Ag/AgCl} + E^{o}_{Ag/AgCl} + 0.59pH \qquad (1)$$

where $E_{Ag/AgCl}$ is the experimental measured potential and $E^{o}_{Ag/AgCl}$ is the standard potential of Ag/AgCl reference electrode against the NHE (0.196 V).

Incident photon to current conversion efficiency (IPCE) measurements were carried out using a white LED (TLS, Zahner) coupled with an USB controlled monochromator between 430-730 nm. During the measurement a constant background light source is maintained and a small light excitation (ca. 10%) was superimposed at 0.2 Hz. The data were collected every 10 nm and simulated curves were obtained using the CIMPS software.

Mott-Schottky analysis: Electrochemical impedance (EIS) measurements were performed in three electrode configuration. The potential was scanned from -0.8 to +0.5V vs. Ag/AgCl with 50 mV increments and equilibrated for 30 s at each potential. The area of the electrode exposed to the electrolyte was 0.785 cm2. Impedance data were collected using 10 mV ac amplitude at three frequencies 0.1, 1.0, and 5 kHz. The flat band potential (Vfb) and the donor density (ND) were calculated using Mott-Schottky relationship (eq 2)

$$\left(\frac{1}{C^2}\right) = \frac{2}{eN_D\varepsilon_o\varepsilon_r A^2}\left(V_{fb} - \frac{kT}{e}\right) \qquad (2)$$

where A is the surface area of the electrode, ε_o is the permittivity of free space and ε_r is dielectric constant of hematite, T is the temperature and k is the Boltzmann's constant. EIS measurements were also performed at 0.23 V vs. Ag/AgCl (1.23 V vs RHE) under illumination and the data were fitted with Zview software (Schribner Associatee Inc., Version 3.4)

Results and discussion

Figure 1 shows typical SEM images of ED hematite thin films without and with different organic additives. The morphologies of the films can be tuned by adding 1 mM of the organic additives into the deposition bath. As prepared films without additives feature 'corn flake' structure (Figure 1a inset) which converts to elongated plate like nanoparticles with average lengths of 110-130 nm and diameters of ca. 45-60 nm upon annealing at 600 ^{o}C. Addition of Sds results similar nanoplate morphologies of reduced dimensions, 30-40 nm in diameter and ca. 100 nm in length. This similarity arises due to very weak interaction of Fe^{+2} and sulfonate in the presence of excess carboxylate ions in the electrolyte. Films with GA are composed of 'worm' like aggregates of domain size ranging 220-330 nm after thermal treatment. The aggregates have branches and beneath these aggregates there are round shaped nanoparticles with diameters of 40-60 nm C343 containing films consist of nanoplates of ca. 50-60 nm which are sintered together. Different capping agents (CH_3COO^-, F^-, Cl^-, $C_2H_8N_2$) are used to control the shape and morphologies of electrodeposited metal oxides films such as ZnO, Cu_2O, α-FeOOH.[43-45] In general these capping agents can preferentially adsorbed on certain crystal planes and block or slow down the growth which results anisotropic growth. As the applied potentials, the concentrations of acetate and Fe ions are kept constant in the current study the morphology varaitions likely arises from the organic additives and similar mechanism can be envisaged. The films are smooth and homogeneous over wide areas and have good adhesion to the FTO support without any cracks. (Figure 1S, supporting info). On the other hand, the film thickness is controlled by the used deposition potential and time. A linear increase of absorbance with the deposition time is observed (Figure 2Sa). There is a slight variation of film thicknesses according to the type and concentration of the organic additive. Films without organic additives (Fe_2O_3) have a thickness of 150-160 nm and those with additives are with 140-150 nm slightly thinner as evidenced from cross sectional SEM (Figure 1b inset). The amount of the photoactive material is cross-checked spectrophotometrically by dissolving the same area of the films in 2M HCl solution and following the absorbance of $[FeCl_4]^-$/ $[FeCl_2]^+$ complex at 340 nm (Figure 2S b-c). [46] The amount of 'FeOOH' deposited by passing 0.30 C is estimated to be 0.17-0.20 mg which gives a deposition efficiency of 75-82 %. The deposition time varies to have the same amount of charge and it increases in the order of Fe_2O_3/C343 > Fe_2O_3/GA > Fe_2O_3/Sds > Fe_2O_3. This suggests that the organic additives decrease the rate of film formation either by adsorbing or forming soluble complexes which compete with the film growth.

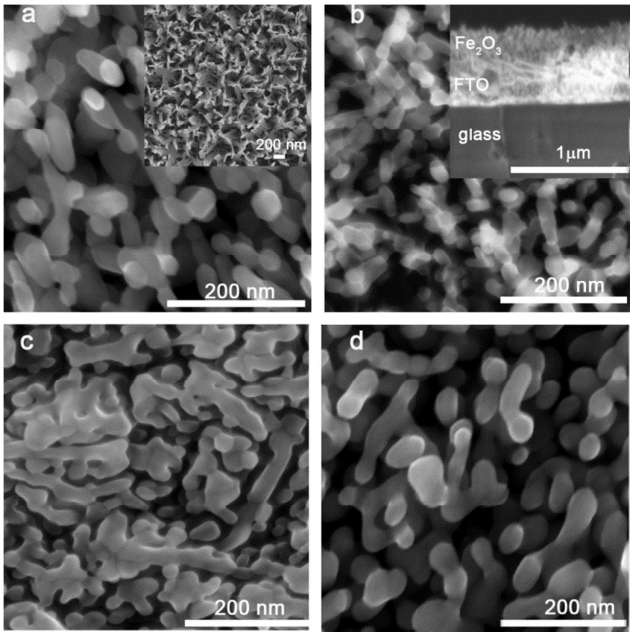

Figure 1. SEM images of Fe_2O_3 films electrodeposited in 3 min at 0.4 V vs Ag/AgCl and annealed at 600 ^{o}C: (a) without additives (Fe_2O_3) and in the presence of (b) 1 mM Sds (Fe_2O_3/Sds), (c) 1 mM GA (Fe_2O_3/GA)), and (d) 1 mM C343 (Fe_2O_3/C343). Insets are (a) as prepared Fe_2O_3 films and (b) cross-sectional view of Fe_2O_3 films.

The UV-vis absorption spectra of the annealed films are obtained both in absorbance and diffuse-reflectance mode. As deposited films with additives display light yellow colour and turn orange after annealing. The films without additive appear in general more reddish. All films exhibit similar absorption features (Figure 2). Typically, a shoulder at 540 nm and a peak between 380-400 nm are observed, which are characteristics of Fe_2O_3 films and originate from indirect Fe 3d to 3d and direct O 2p to Fe 3d transitions. [47] The optical band gap is calculated by converting the respective diffuse-reflectance spectra into Tauc plots (Figure 1Sd). Values of 2.10-2.15 eV were obtained by fitting data points near the absorption onset for indirect band gap transition. These values are in good agreement with other reported values for Fe_2O_3. [35,37]The Fe_2O_3/GA and Fe_2O_3/C343 films exhibit slightly extended absorption in the region 400nm to 500 which may be due to the larger grain sizes of the films.

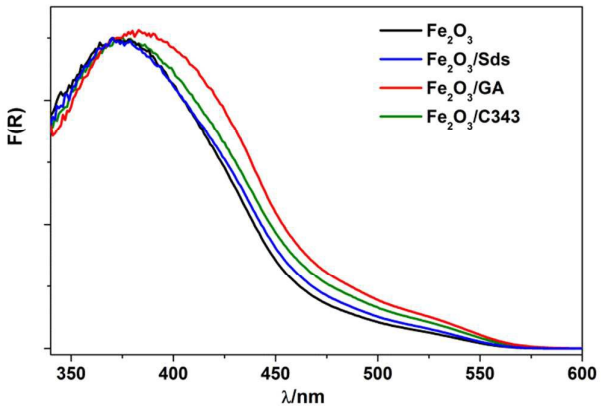

Figure 2. UV-vis spectra of α-Fe_2O_3 with and without the organic additives.

Figure 3a compares the X-ray diffraction patterns of films with and without organic templating agents after thermal treatment at 600 °C. The formation of the hematite phase is evidenced by comparison of standard α-Fe_2O_3 XRD patterns (PDF 99-000-0131) with the peaks associated with the films. We observe reflexes associated with (012), (110) and (024) planes of which the intensity of (110) is highest. This suggests the Fe_2O_3 films have a preferred (110) orientation which favours higher electron conductivity. [48] Additionally, looking at the ratio of the peaks FWHM ((110)/(024)) of the films, values of 0.86, 0.72, 0.95 and 0.90 are obtained for Fe_2O3, Fe_2O_3/Sds, Fe_2O_3/GA and Fe_2O_3/C343, respectively. The result suggests GA and C343 containing films have large fraction of crystals which are oriented in 110 plane. This will affect significantly the measured photocurrents (see below). Furthermore, as-prepared films are amorphous and no noticeable reflections are observed except those arising from the FTO substrate.

As can be seen from the XRD reflexes the hematite peaks are dominated by FTO reflexes and further analysis on the XRD patterns is difficult. To get further structural insights we performed Raman measurements as Raman is inherently a surface sensitive method. The as prepared films indicated as 'Fe-OOH' (Figure 3b bottom) show two characteristic peaks at 245 and 377 cm^{-1} and these peaks match to the two intense peaks of γ-FeOOH.[49] Annealed hematite films show seven Raman peaks at 227, 246, 293, 412, 498, 613, and 1320 cm^{-1} and all can be indexed to reported hematite peaks. [50-51] Additionally, weak peaks at 558 and 1100 cm^{-1} are also observed which belong to the FTO substrate. The absence of the peak at 660 cm^{-1} which is characteristic for Fe_3O_4, suggests our hematite films are pure and agrees well with the XPS measurements (see below). The features of the Raman lines such as peak intensity, broadness or narrowness of the line give information relating grain size and degree of crystallinity. In general the full width at half maximum (fwhm) increases as the feature size of the crystals decreases due to phonon confinement.[50] For the most intense peak at 294 the fwhm is slightly varied between films, being 12.1 10.6, 11.3 and 11.2 cm^{-1} for Fe_2O_3, Fe_2O_3/Sds, Fe_2O_3/GA, and Fe_2O_3/C343.This partly suggests the organic additives result larger crystal sizes as indicated in the SEM. Additionally, the ratio of peak intensities (498/294) show highest value for Fe_2O_3/GA (0.48) compared to Fe_2O_3/Sds (0.38) indicating high degree of crystallinity for GA modified hematite electrodes.

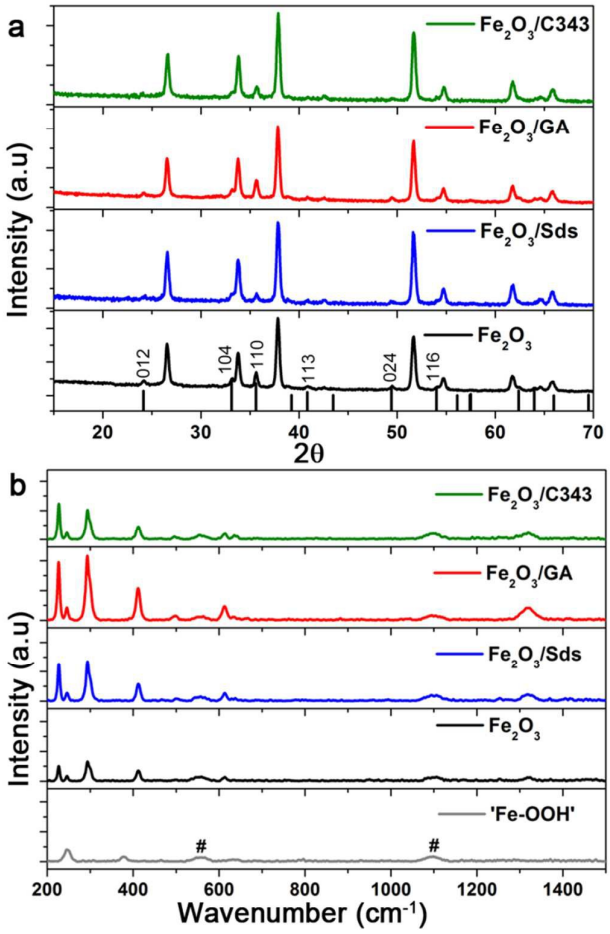

Figure 3. X-ray diffraction patterns (a) and Raman absorption bands (b) of α-Fe_2O_3 films electrodeposited at 0.4 V vs. Ag/AgCl for 3 min and annealed at 600 °C. Signals from the FTO substrate are indicated by number sign.

XPS measurements were performed in order to determine the oxidation state of Fe and to verify the incorporation of the organic additives in the films. The XPS spectra presented in Figure 4 show the Fe $2p_{2/3}$ peaks for as-prepared films and Fe_2O_3 films after annealing. Annealed films exhibit peaks located at 710.5 eV and 709.5 eV being consistent with Fe^{3+} ions in hematite. The weak satellite peak 8 eV above the main $2p_{3/2}$ line provides additional evidence for the Fe^{3+} state which is consistent with previously reported values. [52] The Fe $2p_{3/2}$ peak for the as-prepared samples is slightly shifted towards higher binding energies and centred at 710.9 eV indicating the formation of Fe hydroxides. The O1s peaks also indicate the formation of Fe_2O_3 (Figure 3Sa). The C:Fe atomic ratios were estimated from C1s (C-O) and Fe 2p peaks; for the as-prepared films values of 0.48 and 0.34 were obtained for 'FeOOH' films with and without the organic additive GA, respectively. As the films were prepared from acetate containing electrolyte the inclusion of considerable amount of C is expected.

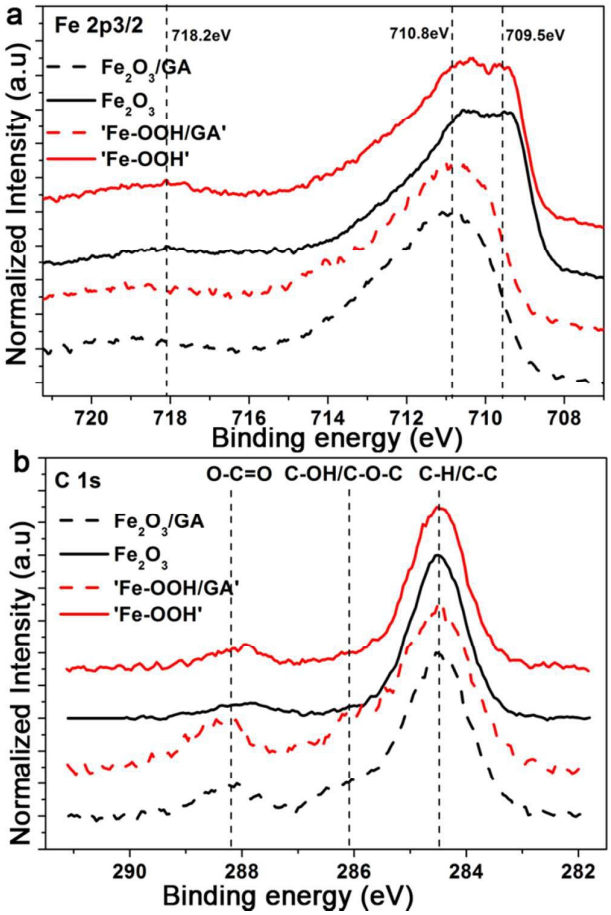

Figure 4. XPS spectra of Fe_2O_3 films electrodeposited without and with GA showing the (a) Fe 2p and (b) C1s regions films, respectively.

However, the difference in the C content indicates the successful incorporation of the organic additives to the film. However, after annealing majority of the C will decompose and burn out. The weak peak observed around 288.2 eV is related to C1s (O-C=O) as adsorbed carbonate species also appear in the same region unambiguous assignment would be difficult. Additionally, the peak intensities are comparable and the absence of C1s (Fe-C) which appear at low binding energy compared to C1s reference peak also support there is no preferential doping effect from the organic additives. We also investigate the possible N doping effect arising from Fe source or from the addition of C343, the survey spectra collected for Fe_2O_3/GA and Fe_2O_3/C343 show no traces of N (Figure 3Sb). This suggests C343 does not induce N doping and the observed photocurrent difference.

The photoelectrochemical activities of the films were investigated using current-voltage curves, chopped light voltammetry and IPCE measurements. Since there is no significant photoelectrochemical activity for films annealed below 600 ^{o}C, all photoelectrochemical measurements were performed for films annealed at this temperature. Figure 5 shows current voltage curves of hematite films under light illumination from a white LED with 100 mW cm^{-2}. The potential was scanned from -0.4 V to +1 V vs. Ag/AgCl at a scan rate of 10 $mV^{-1}s$. The onset of the dark photocurrent for all electrodes is around 1.7 V vs. RHE and no significant variation is observed (Figure 5 solid lines). Under illumination the photocurrent is negligible below 1.0 V vs. RHE and starts to rise only above 1.0 V. As the bias potential increases anodically, the photocurrent shows a significant increase and continues increasing up to the dark current onset at 1.7 V. The magnitude of the photocurrent slightly depends on the direction of illumination (front vs. back side illumination) for all electrodes except Fe_2O_3/GA. In the case of Fe_2O_3/GA there is a marked difference in photocurrent between the fronts vs. back side illuminations (Figure 5c dashed line vs dashed dotted line). A significant enhancement was observed under back side illumination even though there is a loss in light intensity due to the FTO. Back side illumination is preferable because the pathway for electrons to the high conducting FTO is shorter. But effective photocurrents can only be obtained if the electrode is porous enough to allow suitable electrolyte penetration. The obtained result suggests that especially the Fe_2O_3/GA electrode provides the needed high porosity which allows the easy penetration of the electrolyte thereby decreasing the diffusion pathway for the photogenerated electron/hole pairs. Our observation agrees with a recent report by Toussaint et.al which shows the effect of illumination direction for mesoprous Fe_2O_3 films formed by soft templating in a sol-gel route [53]. However, the other organic additives (Sds as well as C343) appear to lead to relatively compact hematite films for which only electron/hole pairs generated at the electrolyte semiconductor interface are effectively collected irrespective of the direction of illumination.

Comparison of the photoanode performance of the different electrodes shows that Fe_2O_3/GA exhibits the highest photocurrent which is followed by Fe_2O_3/C343. The photocurrent of the unmodified Fe_2O_3 is higher than Fe_2O_3/Sds which exhibits the lowest photocurrent of all. Evidence is given by Raman measurement showing for the Fe_2O_3/Sds a lower degree of crystallinity likely combined with an increased number of grain boundaries. The low photoresponse of

Fe_2O_3/Sds is probably due to charge recombination at these grain boundaries. At an applied potential of 1.40 V vs. RHE the photocurrent at Fe_2O_3/GA is 5-6 times higher than those achieved at the unmodified Fe_2O_3. The obtained photocurrents are generally small compared to the state-of-the-art APCVD hematite films [15] but comparable with those recently reported value by Fu et al. in which ethylene glycol was used as additive for ED of hematite films.[54]

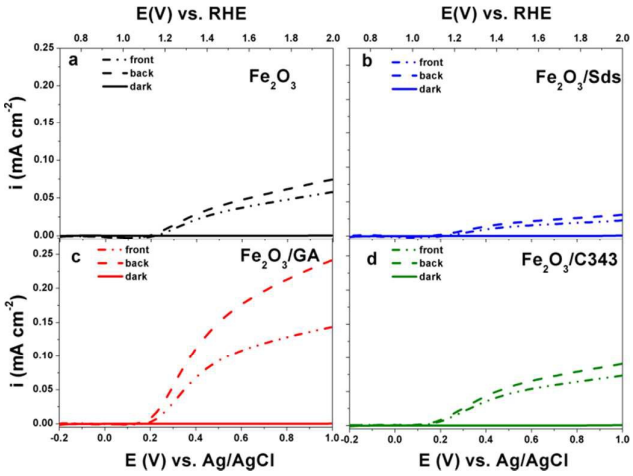

Figure 5. (a) I-V curves of measurement of ED Fe2O3 films without and with organic additives in 1 M NaOH showing the effect of light illumination directions.

The photoactivity differences between the different hematite films become more evident when an effective hole acceptor molecule is used during the photoelectrochemical experiments. H_2O_2 is used as probe molecule to evaluate the efficiency and the kinetic limitations of different photoanodes as the oxidation of H_2O_2 is kinetically much easier than water oxidation. [55-56] We performed photoelectrochemical experiments in the presence of 0.5 M H_2O_2 (Figure 4Sa-b). The anodic photocurrent is significantly increased and the onset of the photocurrent is shifted to a value close to the flat band potential of hematite photoanode. The photoactivity of the electrodes can be easily compared by calculating the hole transfer efficiency taking the photocurrent ratios measured without and with H_2O_2 at a given bias potential (Figure 6a). The result clearly shows that the organically modified hematite electrodes, particularly Fe_2O_3/GA, outperform those prepared in the absence of the additives. When the kinetic barrier for the oxidation reaction is removed the variation in the activity of the different electrodes arise from the influence of the organic molecules on the morphology of the films leading to better charge separation or hole transfer to the solution.

In light of the above results we attempted to improve the photoresponse of Fe_2O_3/GA by preparing Fe_2O_3 electrodes from a bath containing different concentrations of GA. As the concentration of GA increased from 1 mM to 6 mM the photo current slightly decreases under back side illumination (Figure 6b). The SEM images of Fe_2O_3/GA with different concentration presented in Figure 5S shows similar morphologies. However, there are differences the way the grain domains interconnected. As the GA concentration increases the domains are becoming large and loosely packed. This probably leads to photocurrent loss due to reduced available reaction sites and the need by charge carriers to travel longer distance to reach the interface. Based on this results further experiments were conducted on electrodes prepared from solutions containing 1 mM GA.

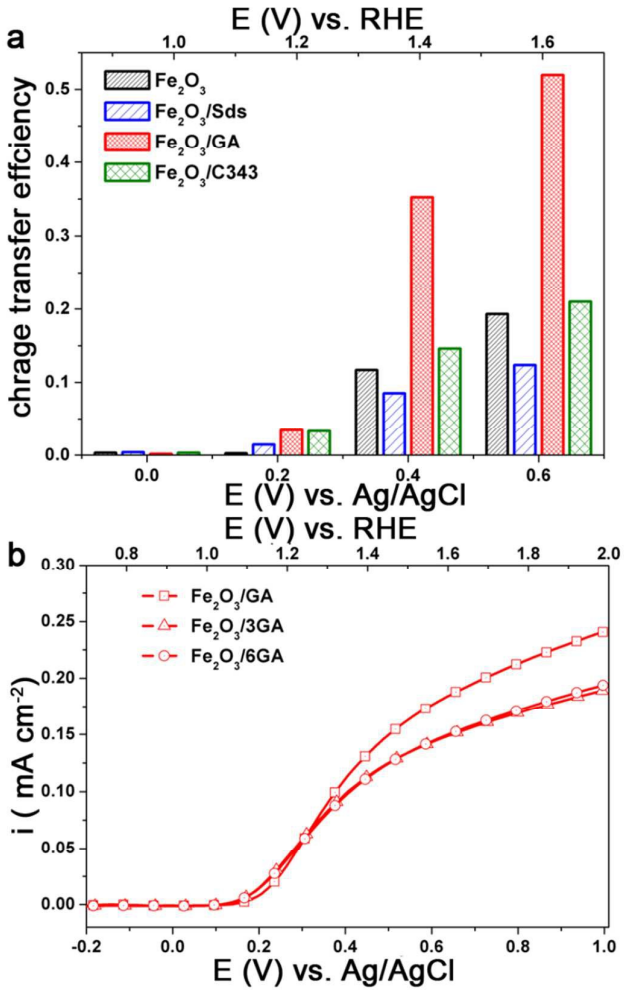

Figure 6. (a) Charge transfer efficiency calculated taking the ratio of photocurrent densities (i_{H2O}/i_{H2O2}), (b) effect of GA concentration on the photocurrent under back side illumination.

Effect of Ti treatment

Ti doping has been shown to improve the performance of hematite photoanodes significantly and the role of Ti is attributed controlling the crystal size and in some cases leading to a preferential orientation of the crystals. [57] On the other hand, a thin underlying TiO_2 layer improves the photoresponse of hematite electrodes by blocking the electron hole recombination. [58] Following a simple and facile post treatment procedure reported by Franking et al. [18] the hematite photoanodes were treated with 20 µL of 25 mM $Ti(OBu)_4$ and dried in air prior to annealing. Higher concentrations of $Ti(OBu)_4$ were tested but the optimum was 25 mM and data are presented for the optimized concentration. The Ti treatment has no significant influence on

the morphology of the films, but the presence of Ti is confirmed by EDXS (Figures 4Sc and d).

Figure 7a shows the current voltage behaviour of Ti treated hematite photoanodes under light illumination. The photocurrent increases significantly and the onset of the photocurrent shifts ca. 30 mV cathodically for Fe_2O_3 and Fe_2O_3/GA after Ti loading (Figure 6b). The photocurrent density at 1.4 V RHE increased by a factor of 2 for Fe_2O_3/GA/Ti (0.20 $mAcm^{-2}$) and for Fe_2O_3/C343/Ti (0.12 mA cm^{-2}), respectively. Both Fe_2O_3/Ti and Fe_2O_3/Sds/Ti show a pronounced photocurrent density of 0.12 $mAcm^{-2}$ and 0.06 $mAcm^{-2}$, respectively, which is 4-5 fold higher than without Ti treatment. The Ti treatment has modest influence on Fe_2O_3/GA and Fe_2O_3/C343 electrodes than Fe_2O_3 and Fe_2O_3/Sds electrodes, respectively. This shows the organic additives GA and C343 form already hematite morphologies with less grain boundaries so that the Ti treatment is of less importance. Interestingly, the Fe_2O_3/GA/Ti photoanode still maintains higher photocurrent density which is 1.6 times higher than for Fe_2O_3/Ti. Previous studies on surface modification of hematite photoanodes with very thin oxide over layers (Ga_2O_3 and Al_2O_3) demonstrated improved photoresponses. [59-60] The role of the oxide over layers attributed to surface states passivation which act as recombination centres or hole traps. Thus in the presence of the oxide over layers reduced capacitive response (due to charging of surface states) is expected. Following the method of Bertoluzzi et.al [61] we performed cyclic voltammetry (CV) investigations on Ti modified Fe_2O_3 and Fe_2O_3/GA electrodes to ascertain the function of Ti oxide over layer. The electrodes are first polarized at higher anodic potential (1.8V vs. RHE) under illumination and cyclic voltammograms are recorded at different scan rates. As shown in Figure 6S a and c, only one cathodic capacitive peak is observed without the accompanying anodic peak which show the hematite films are suffering from high recombination (as Bertoluzzi et. described in detail). But after Ti treatment (Figure 7S b and d) the corresponding anodic peak is partially recovered and the magnitude of the cathodic peaks reduced. The cathodic peak current measured at 50 mv/sec reduced from 16.2 to 6.3 µA cm^{-2} and from 8.7 to 4.9 µA cm^{-2} for Fe_2O_3 and Fe_2O_3/GA electrodes after Ti treatment, respectively. The evolution of the anodic peak is an indication that the Ti oxide over layer facilitates charge detrapping during the reverse scan. The peak capacitive current is linearly increases with scan rate (Figure 7S a-d inset) which suggest the current is not diffusion controlled. The improved photoactivity brought by Ti treatment is probably attributed to passivation of grain boundaries (trap states).

Effect of Co-Pi treatment

Cobalt phosphate (Co-Pi) has been extensively studied as an alternative and cheap oxygen evolution catalyst (OER) catalyst compared to catalysts including more rare elements such as IrO_2 and RuO_2. [62-63] It has been proven as effective water oxidation co-catalyst in several oxide-based PEC systems. Thus, Co-Pi was deposited on Ti-doped hematite electrode by electrodeposition at 0.9 V vs. Ag/AgCl for 210 s form a phosphate buffer solution containing 0.5 mM $Co(NO_3)_3$. Figure 7b shows the selective photocurrent densities obtained on Fe_2O_3 and Fe_2O_3/GA electrodes after Ti and Co-Pi treatment. After the Co-Pi treatment the photocurrent density at 1.4 V vs. RHE was increased to 0.53 mA cm^{-2} and 0.48 mA cm^{-2} for Fe_2O_3/GA and Fe_2O_3, respectively. Remarkably, the onset of the photocurrent is cathodically shifted by ca. 50-70 mV for both electrodes. This confirms the role of Co-Pi as a catalyst which facilitates the hole transfer and reduces surface recombination. [61, 64-65] The treatment of Ti and Co-Pi also improves the photocurrent of Fe_2O_3/Sds (0.25 mA cm^{-2}) and Fe_2O_3/C343 (0.27 mA cm^{-2}) electrodes, respectively (Figure 6Sa)

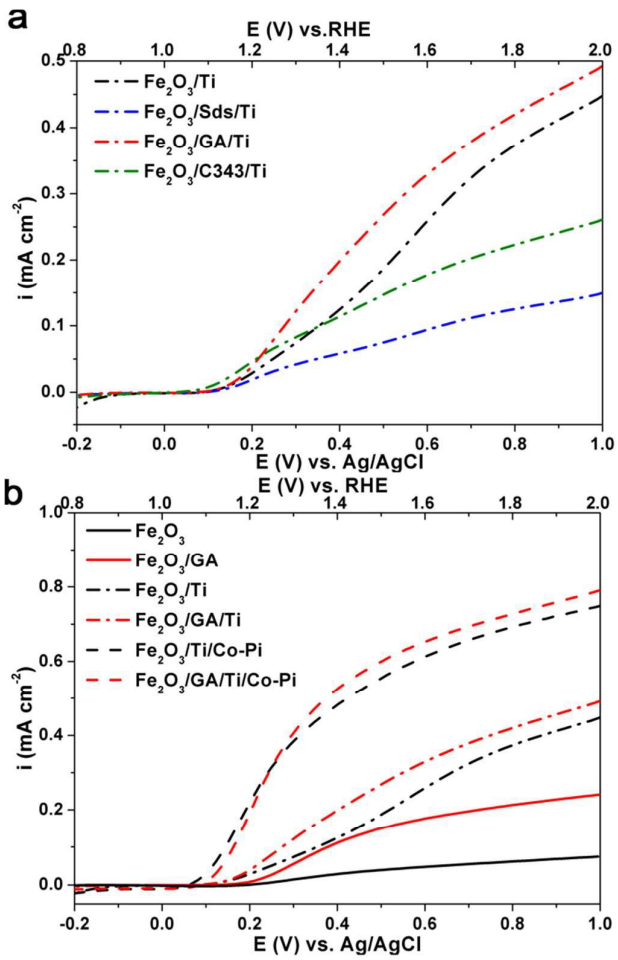

Figure 7. Effect of Ti and Co-Pi treatment: (a) I-V curves of Ti doped ED Fe_2O_3 films without and with organic additives in 1 M NaOH and (b) I-V curves showing the shift of the onset for Fe_2O_3 and Fe_2O_3/GA after loading of Ti and Co-Pi.

IPCE measurements

The incident photon to current conversion efficiency (IPCE) of electrodeposited hematite films were measured changing the direction of illumination (Figure 8). In general the IPCE spectra follow the absorption spectra of the films (Figure 2) very well but they decrease more rapidly at longer wavelength. The IPCE values also demonstrate that the hematite films with the organic additives, with the exception of Fe_2O_3/Sds, are able to

convert the absorbed photons into current more effectively than the Fe_2O_3. As observed in I-V curves in Figure 8 the back side illumination results higher IPCE values particularly in the short wavelength regime. The penetration depth of the high energy photons is much shorter and creates electron hole pairs at the FTO/hematite interface which is remote from the hematite/solution interface and hence the majority of them is lost through recombination and does not contribute to the photocurrent.

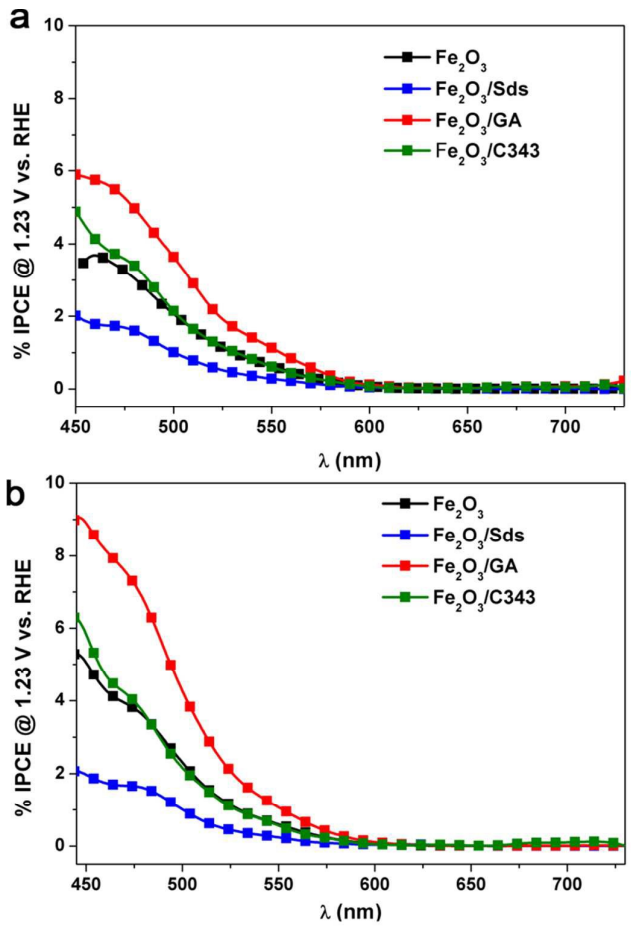

Figure 8. IPCE spectra of Fe_2O_3 films deposited without and with additives (a) front and (b) back side illumination

Thus back side illumination results in lower photocurrent (less IPCE) compared to front side illumination and the situation is prevailing if the hematite layer is compact and/or thick.[15] However, if the hematite layer exhibit certain degree of porosity which extends to the FTO back contact, back side illumination is beneficial as the holes from the high energy photons have the chance to reach electrolyte and participate in the oxidation process.[53] Indeed this is the case for Fe_2O_3/GA electrodes which show much increased IPCE values under back side illumination. Note worth mentioning the highest IPCE value achieved 8.5 % for Fe_2O_3/GA at 470 nm which is twice the value obtained on Fe_2O_3 showing the superior activity of GA modified hematite electrodes.

Mott-Schottky (MS) and Electrochemical impedance spectroscopy (EIS) analysis

To gain further insights of the effect of organic additives and doping on the photoactivity of ED hematite films we conducted EIS and MS analysis. The donor densities and the flat band potentials of semiconductor electrodes can be accurately estimated from MS plots using eq (2) if the electrode is planar and no surface state are involved. Considering the morphologies and the sizes of the hematite grains, both criteria cannot be met with any of the electrodes under investigation. The situation is directly manifested by a strong frequency dependence of the complex impedance and the curved nature of the MS plots (Figure 9 a-d). Therefore the determination of the donor densities from the slope of these curved MS plots is very unreliable. Similar type of behaviour was reported for sputter deposited and powder pressed hematite photoanodes. [66-67] However, the intercept is fairly similar for the measured frequencies and can be used to estimate the flat band potentials. The plots are fitted in the range of 0.4 V- 0.7 V vs RHE and the values obtained are 0.53 ± 0.02 V, 0.61 ± 0.05 V, 0.49 ± 0.02 V, 0.54 ± 0.05 V for Fe_2O_3, Fe_2O_3/Sds, Fe_2O_3/C343, and Fe_2O_3/GA, respectively. The values obtained are close to the onset of the photocurrent in the H_2O_2 solution measured under chopped light illumination which is 0.53-0.55V. (Figure 3Sb). Reported hematite flat band potentials range between 0.4 and 0.6 V vs. RHE and thus our values coincide with it. [54,56,68] After the Ti treatment the MS plots become more flat (Figure 6Sb) indicating an increase in donor density, however, extracting the flat band potentials and the donor densities quantitatively is not possible.

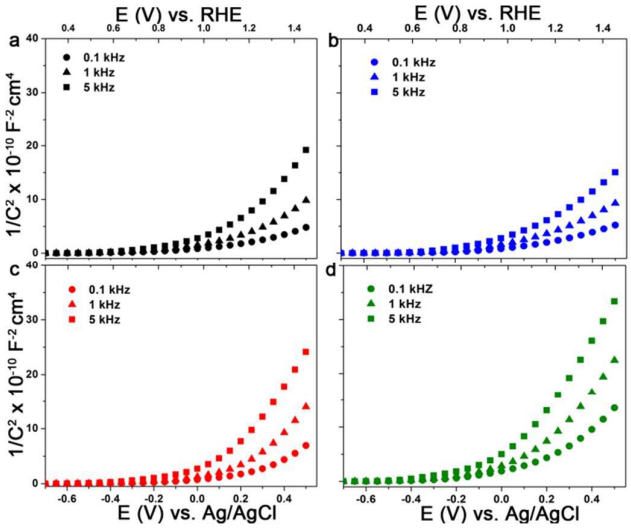

Figure 9. MS plots of ED Fe_2O_3 films without and with organic additives 1M NaOH (a) Fe_2O_3 (b) Fe_2O_3/Sds, (c) Fe_2O_3/GA and (d) Fe_2O_3/C343 at the indicated frequencies.

Figure 10a-b show the Nyquist plots for Fe_2O_3 and Fe_2O_3/GA obtained from measurements under illumination at 1.23 V vs. RHE for electrodes before and after loading of Ti and Co-Pi. The plots consist of two semi-circles at bias potentials < 1.4 V vs. RHE which is consistent with the behaviour of hematite photoanodes under illumination. [24] The experimental data

were fitted to an equivalent circuit model consisting of two RC units each containing a resistance in parallel with a constant phase element (CPE) (Figure 9a inset). [68-69] In this model the CPE replaces the pure capacitive elements to account the non-ideal behaviour originated from non-homogeneity of the films and roughness. The model consists of the space charge capacitance for bulk hematite (CPE1) and surface state capacitance (CPE2). R_1 and R_2 represent the resistance of the bulk hematite and charge transfer resistance from the surface states to the solution, respectively. The series resistance R_s accounts for resistance of the TCO and/or the electrolyte. The fitted data were collected and summarized in Table 1.

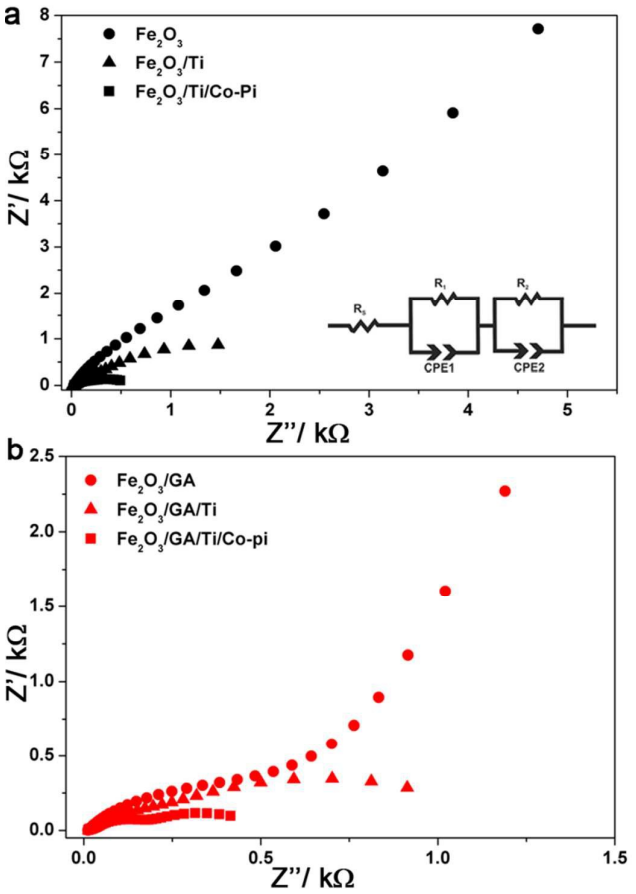

Figure 10. EIS results and analysis: Effect of Ti and Co-Pi loading on the complex impedance plots of (a) Fe_2O_3 and (b) Fe_2O_3/GA. The inset shows the equivalent circuit model used for fitting the data

The organic additive GA, greatly reduces the charge transfer resistance (R_2) responsible for the water oxidation reaction due to a favourable morphology which allows easy penetration of the electrolyte. The larger grain sizes due to fused nanoparticles lead to less grain boundaries. Doping with Ti further reduces R_2 indicating facilitated charge transfer from the hematite surface to the solution. Notably, the resistance of the bulk hematite (R_1) is affeted and after Ti treatment the value is reduced by a factor of about four for both electrodes which further supports the Ti incorporation into the bulk of the film during the drop cast procedure. The Co-Pi treatment slightly decreases the bulk resistance and greatly reduces the charge transfer resistance and increases the surface state capacitance resulting high photocurrent densties.

Table 1: EIS data obtained by fitting the equivalent circuit model in the frequency range 1Hz and 1.2 kHz (Figure 10a inset)

Electrodes	R_s/Ω	R_1/Ω	R_2/Ω	CPE1/µF	CPE2/ µF
Fe_2O_3	17.7	825	98533	18.1	26.7
Fe_2O_3/GA	13.9	730	35946	27.4	82.7
Fe_2O_3/Ti	19.2	200	2493	31.8	58.8
Fe_2O_3/GA/Ti	20.9	155	1235	28.3	175.1
Fe_2O_3/Ti/Co-Pi	32.5	145.2	430	58.1	370.3
Fe_2O_3/GA/Ti/Co-Pi	22.9	150	303	41.5	408.2

Conclusion

In summary, we have shown that the use of small organic molecules tunes the size and morphology of electrodeposited hematite thin films inducing enhanced photoactivity The improved photoelectochemical activity of the organically modified hematite films can be attributed to a favorable film morphology which allows easy penetration of the electrolyte and better charge separation. Better accessibility of the electrolyte is demonstrated by a dependence of photocurrent and IPCE on the direction of illumination. However, the functionality of the the organic additives govern the type and strength of interactions as sulfonates impart no unique morphology as opposed to the carboxylate ligands. Comparison of the photocurrent density at 1.4 V vs. RHE shows that the Fe_2O_3/GA electrode displays a photocurrent density 5-6 times higher than that of Fe_2O_3. The photocurrent density can be further enhanced by the loading with Ti dopant and Co-Pi OER co-catalyst, respectively, observable in a cathodic shift of the onset of the photocurrent. The main role of the organic additive, specifically GA, is reducing the charge transfer resistance from the hematite surface to the solution which is the kinetic bottleneck for the overall water splitting reaction, as evidenced by EIS. There is no need that the organic additives impart preferential crystal orientation and ordering in the resulting films.

Acknowledgements

This work is supported by the Deutsche Forschungsgemeinschaft (DFG) (WA 1116/23-1) within the priority program SPP1613. We are very grateful to Dr. Carsten Dosche for his help during the additional XPS experiments.

References

1. A. Maczulka, *Renewable energy Sources: Sources and Methods*, Library of Congress Cataloging, 2010, Chapter 5.
2. A. Fujshima, K. Honda, *Nature*, 1972, **238**, 37–38.
3. M. Graetzel, *Nature*, 2001, 414, 338-343.
4. O. Khaselev, J. A. Turner, *Science*, 1998, **280**, 425-427
5. M. G. Walter, E. L.Warren, J. R. McKone, S. W. Boettcher, Q. Mi, E. A. Santori, N. S. Lewis, *Chem. Rev.*, 2010, **110**, 6446–6473.

6. Z. Li, W. Luo, M. Zhang, J. Feng, Z. Zou, *Energy Environ. Sci.*, 2013, **6**, 347-370.
7. T. Hisatomi, J. Kubota, K. Domen, *Chem. Soc. Rev.*, 2014,**43**, 7520-7535.
8. K. Sivula, F. Le Formal, M. Graetzel, *ChemSusChem.*, 2011, **4**,432-449.
9. M. J. Katz, S. C. Riha, N. C. Jeong, A. B. F. Martinson, O. K. Farha, J. T. Hupp, *Coord. Chem. Rev.*, 2012, **256**, 2521–2529.
10. D. K. Bora, A. Braun, E. C. Constable, *Energy Environ. Sci.*, 2013,**6**, 407-425
11. U. Bjorksten, J. Moser, M. Graetzel, *Chem. Mater.,* 1994, **6**, 858–863
12. A. B. Murphy, P.R.F. Barnes, L.K. Randeniya, I .C. Plumb, I. E. Greyb, M. D. Horne, J.A. Glawsscock, *Int. J. Hydrogen Energy*, 2006, **31**, 1999–2017.
13. J. H. Kennedy, K. W. Frese Jr., *J. Electrochem. Soc.*, 1978, **125**, 709–714.
14. L. Vayssieres, N. Beermann, S-E. Lindquist, A. Hagfeldt, .*Chem. Mater.*, 2001, **13**, 233−235
15. A. Kay, I. Cesar, M. Graetzel, *J. Am. Chem. Soc.*, 2006, **128**, 15714–15721.
16. Y. Lin, S. Zhou, S. W. Sheehan, D. Wang, *J. Am. Chem. Soc.*, 2011, **133**, 2398–2401
17. S. C.Warren, K. Voïtchovsky, H. Dotan, C. M. Leroy, M. Cornuz1, F. Stellacci, C. Hebert, A. Rothschild and M. Graetzel, *Nature Mater.*, 2013, **12**, 812-849.
18. R. Franking, L. Li, M. A. Lukowski, F. Meng, Y. Tan, R. J. Hamers, S. Jin, *Energy Environ. Sci.,* 2013, **6**, 500-512.
19. J. A. Glasscock, P. R. F. Barnes,I. C. Plumb, N. Savvides , *J. Phys. Chem. C*, 2007, **111**,16477–16488.
20. S. S. Yarahmadi, K. G. Upul Wijayantha, A. A. Tahir, B. Vaidhyanathan, *J. Phys. Chem. C.,*2009, **113**, 4768–4778,
21. A. K. Shwarsctein,Y. S. Hu, A. J. Forman,G. D. Stucky, E. W. McFarland, *J. Phys. Chem. C.*, ,2008, **112**, 15900–15907
22. D. K. Zhong, D. R. Gamelin, *J. Am. Chem. Soc.*, 2010, **132**, 4201-4207.
23. S. D. Tilley, M. Cornuz, K. Sivula, M. Grätzel, *Angew. Chem. Int. Ed*., 2010, **49**, 6405–6408.
24. F. Le Formal, N. Tétreault,M. Cornuz, T. Moehl, M. Graetzel, K. Sivula, *Chem. Sci.,* 2011, **2**, 737–743.
25. T. Hisatomi, F. Le Formal,M. Cornuz, J. Brillet, N. Tétreault, K. Sivula, M. Graetzel*, Energy Environ Sci.*, 2011,**4**, 2512–2515.
26. C. D. Park, D. Magana, A. E. Stiegman, *Chem. Mater.,* 2007, **19**, 677–683.
27. S. U. M. Khan, J. Akikusa*, J. Phys. Chem.B*, 1999, **103**, 7184–7189.
28. C. J. Sartoretti, B D. Alexander, R.Solarska, I. A. Rutkowska, J. Augustynski, *J Phys. Chem. B*, 2005, **109**, 13685–13692.
29. A. A. Tahir, K. G. U. Wijayantha, S. S. Yarahmadi, M. Mazhar, V. McKee, *Chem. Mater.*, 2009, **21**, 3763–3772
30. M. Lie, H. Fjellvåg, A. Kjekshus, *Thin Solid Films*, 2005, **488**, 74-81.
31. S. C. Riha, B. M. Klahr, E. C. Tyo, S. Seifert, S. Vajda, M. J. Pellin, T. W. Hamann, A. B. F. Martinson, *ACSNano*, 2013, **7**, 2396-2405.
32. Y. S. Hu,A. K. Shwarsctein, A. J. Forman, D. Hazen, J. N. Park, E. W. McFarland, *Chem. Mater.*, 2008, **20**, 3803–3805
33. Pravin S. Shinde, Geun Ho Go, Won Jae Lee, *J. Mater. Chem.* 2012, **22**, 10469-10471.
34. R. S. Schrebler, L. Ballesteros, A. Burgos, E. C. Munoz, P. Grez, D. Leinen, F. Martin, J. R. Ramos-Barrado, E. A. Dalchiele, *J. Electrochem. Soc.*, 2011, **158**, D500-D505
35. R. Schrebler, K. Belloa,F. Veraa,P. Curya, E. Munoza, R. del Ríoa, H. G. Meiera, R. Córdovaa, E. A. Dalchiele, *J. Electrochem. Soc.,* 2006, **9**, C110-113.
36. R. L. Spray, K. S. Choi, *Chem. Mater.,* 2009, **21**, 3701–3709
37. A. K. Shwarsctein, Y-S. Hu, A. J. Forman, G. D. Stucky, E. W. McFarland, *J. Phys. Chem. C*, 2008, **112**, 15900-15907.
38. P. Kumar, P. Sharma, R. Shrivastav, S. Dass, V. R. Satsangi, *Int. J. of hydrogen energy*, 2011, **36**, 2777-2784
39. Y. Liu, Y. X. Yu, W. D. Zhang, *Electrochimica Acta*, 2012, **59**, 121– 127.
40. X. Shi, K. Zhang, K. Shin, J. H. Moon, T. W. Lee, J. H. Park, *Phys. Chem. Chem. Phys*., 2013, **15**,11717-11722.
41. C. Boeckler, T. Oekermann, A. Feldhoff, M. Wark, *Langmuir,* 2006, **22**, 9427-9427.
42. H. Graaf, F. Lüttich, C. Dunkel, M. Wark, T. Oekermann, *J. Phys. Chem. C*, 2012,116, 5610-5613.
43. M. J. Siegfried, K.-S. Choi,. *J. Am. Chem. Soc. 2006*, **128**, 10356-.10357
44. L. F. Xu, Y. Guo, Q. Liao, J. P. Zhang, D. S. Xu, *J. Phys. Chem. B* 2005, **109**, 13519-15522.
45. S. Jiao, L. Xu, K. Hu, J. Li, S. Gao, D. Xu, *J Phys. Chem. C*, 2010, **114**, 269-273.
46. G.A. Gamlen, D.O.Jordan, *J. Chem. Soc.*, 1953, 435-1443.
47. L. A. Marusak, R. Messier, W. B. White, *J. Phys. Chem. Solids*. 1980, **41**, 981-984.
48. K. M. Ross, D. M. A. Smith, M. Dupuis, *J. Chem. Phys*. 2003, **118**, 6455-6466.
49. D. Delichere, S. Joiret, C. Pallotta, A. Hugot-Le Goff, *J. Electrochem. Soc.,* 1988, **135**, 305-310.
50. D. Bersani, P. P. Lottici, A. Montenero, J. Raman. Spectrosc. 1999, 30, 355-360
51. I. Cesar, K. Sivula, A. Kay, R. Zboril, M. Graetzel, *J. Phys. Chem. C,* 2009, **113**, 772-782.
52. N. S. McIntyre, D. G. Zetaruk, *Anal. Chem.*, 1977, **49**, 1521-1529.
53. C. Toussaint, H. L. Le Tran, P. Colson, J. Dewalque, Bénédicte Vertruyen, B. Gilbert, N. D. Nguyen, R. Cloots, C. Henrist, *J. Phys. Chem. C*, 2015, **119**, 1642−1650.
54. L. Fu, H. Yu,Y. Li,C. Zhang, X. Wang, Z. Shao, B. Yia, *Phys. Chem. Chem. Phys.,* 2014,**16**, 4284-4290.
55. H. Dotan, K. Sivula, M. Graetzel, A. Rothschild, S. C. Warren, *Energy Environ. Sci.,* 2011,**4**, 958-964.
56. I. S. Cho, M. Logar, C. H. Lee, L. Cai, F.B. Prinz, X. Zheng, *Nano Lett.,* 2014,**14**, 24-31.
57. G.Wang, Y. Ling, D. A. Wheeler, K. E. N. George, K. Horsley, C. Heske, J. Z. Zhang, Yat Li. *Nano Lett.,* 2011, **11** 3503–3509.
58. T. Hisatomi, H. Dotan, M. Stefik, K. Sivula, A. Rothschild , M. Grätzel, N. Mathews*, Adv. Mater.,* 2012, 24, 2699−2702
59. F. Le Formal; K. Sivula, M. Graetzel *J. Phys. Chem. C* 2012, **116**, 26707−26720.
60. T. Hisatomi, F. Le Formal, M. Cornuz, J. Brillet, N. Tetreault, K. Sivula, M. Graetzel, *Energy Environ. Sci.* 2011, **4**, 2512−2515
61. L. Bertoluzzi, L. Badia-Bou, F. Fabregat-Santiago, S. Gimenez, .J. Bisquert, *J. Phys. Chem. Lett.* 2013, **4**, 1334−1339
62. M. W. Kanan, Y. Surendranath, D. G. Nocera, *Chem. Soc. Rev.,* 2009, **38**, 109-114.
63. D. K. Zhong, M. Cornuz, K.Sivula, M. Graetzel, D. R. Gamelin, *Energy Environ. Sci.*, 2011, **4**, 1759‑1764.
64. D. K. Zhong, S. Choi, D. R. Gamelin. *J. Am. Chem. Soc.*, 2011, **133**, 18370−18377.
65. L. M. Peter, K. G. U. Wijayantha, A. A. Tahir, *Faraday Discuss.,* 2012, **155**, 309−322
66. F. A. Benko, J. Longo, F. P. Koffyberg, *J. Electrchem. Soc.,* 1985, **132**, 609-613
67. C. D. Bohn, A. K. Agrawal, E. C. Walter, M. D. Vaudin, A. A. Herzing, P. M. Haney, A. A. Talin, V. A. Szalai, *J. Phys. Chem. C.,* 2012, **116**, 15290-15296.
68. B. Klahr, S. Gimenez, F. Fabregat-Santiago, J. Bisquert, T. W. Hamann, *Energy Environ. Sci.,* 2012, **5**, 7626-7636.
69. J. Y. Kim, J-W. Jang, D. H. Youn, J. Y. Kim, E. S.Kim , J. S. Lee, *RSC Advances*, 2012, **2**, 9415-9422.

Electrochemical deposition of Fe_2O_3 in the presence of organic additives: A route to enhanced photoactivity

Dereje H. Taffa[a], Ines Hamm[b], Christian Dunkel[a], Ilya Sinev[b], Detlef Bahnemann[c], Michael Wark[a]

TCO